



click for updates

Cite this: *Lab Chip*, 2015, 15, 1168

Inertial focusing of spherical particles in rectangular microchannels over a wide range of Reynolds numbers†

Chao Liu,^a Guoqing Hu,^{*a} Xingyu Jiang^b and Jiashu Sun^{*b}

Inertial microfluidics has emerged as an important tool for manipulating particles and cells. For a better design of inertial microfluidic devices, we conduct 3D direct numerical simulations (DNS) and experiments to determine the complicated dependence of focusing behaviour on the particle size, channel aspect ratio, and channel Reynolds number. We find that the well-known focusing of the particles at the two centers of the long channel walls occurs at a relatively low Reynolds number, whereas additional stable equilibrium positions emerge close to the short walls with increasing Reynolds number. Based on the numerically calculated trajectories of particles, we propose a two-stage particle migration which is consistent with experimental observations. We further present a general criterion to secure good focusing of particles for high flow rates. This work thus provides physical insight into the multiplex focusing of particles in rectangular microchannels with different geometries and Reynolds numbers, and paves the way for efficiently designing inertial microfluidic devices.

Received 14th October 2014,
Accepted 22nd December 2014

DOI: 10.1039/c4lc01216j

www.rsc.org/loc

Introduction

Microfluidic techniques are effective tools for manipulation and detection of particles or cells. Many active techniques resorting to external fields for bioparticle separation/manipulation have been developed, such as dielectrophoresis,^{1–3} magnetophoresis,⁴ acoustophoresis^{5,6} and so on. Recently, inertial focusing has been intensively involved in the separation,^{7–14} focusing,^{7,15–18} filtration,^{10,19–23} enrichment,^{12,24,25} and hydrodynamic stretching^{26,27} of particles or cells for biochemical, environmental and biomedicine applications. Due to the intrinsically increasing intensity with the flow velocity, inertial microfluidic devices work passively at a high throughput. Inertial microfluidic devices can employ various channel structures for different functions. Straight channels with fine-tuned aspect ratios^{14,22,28} or microstructures^{15,18,29} are frequently used as particle focusers by reducing the focusing positions. Straight channels have the best parallelizability and the simplest design rules among all structure types. Expansion–contraction,^{11,30,31} serpentine,^{7,9,10} and spiral channels^{12,13,32–34} are widely employed for particle/cell

separation and sorting: the structure can be finely engineered to achieve a balance between the drag force from the structure-induced secondary flows and the inertial lift, making particles occupy size-dependent equilibrium positions. Previously our group successfully demonstrated the inertial focusing and separation of particles and circulating tumor cells (CTCs) using double spiral microchannels in a label-free manner with high separation efficiency and throughput.^{12,13} Despite the intense attention on the devices and applications, some fundamental issues of inertial focusing, *e.g.*, the number and stability of equilibrium positions, remain to be elucidated for efficient designing of inertial microfluidic devices.

Inertial focusing was initially discovered in a macroscale tube flow by Segré and Silberberg.³⁵ Particles can counterintuitively migrate across streamlines to specific equilibrium positions in a finite Reynolds number shear flow, resulting from the nonlinear effect of fluid inertia.^{36–40} Briefly, the inertial migration is attributed to a balance of two effects: (1) the shear-gradient-induced lift arising from the curvature of the Poiseuille flow that drives the particle towards the wall, and (2) the wall-induced lift that pushes the particle away from the wall.

Microchannels fabricated by the planar soft-lithography methods commonly have square or rectangular cross-sections. In contrast to a tube flow, in which the focusing of particles can be explained by the sole force balance in the radial direction,⁴¹ the particles in square and rectangular microfluidic channels behave in a more complicated manner.^{19,21,42–45} In square microchannels, four or eight equilibrium positions

^a State Key Laboratory of Nonlinear Mechanics, Institute of Mechanics, Chinese Academy of Sciences, Beijing 100190, China. E-mail: guoqing.hu@imech.ac.cn

^b Beijing Engineering Research Center for BioNanotechnology & CAS Key Laboratory for Biological Effects of Nanomaterials Nanosafety, National Center for Nanoscience and Technology, Beijing 100190, China.

E-mail: sunjs@nanoctr.cn

† Electronic supplementary information (ESI) available. See DOI: 10.1039/c4lc01216j

have been observed at various values of blockage ratio κ ($\kappa = a/H$, where a is the particle diameter and H is the channel height) and Reynolds number Re ($Re = \rho_f U_{\max} H / \mu$, where U_{\max} is the maximum channel velocity, ρ_f is the fluid density and μ is the dynamic viscosity).^{19,21,44,45} In rectangular microchannels, many research groups have reported two equilibrium positions centered at the two long walls when the aspect ratio AR ($AR = W/H$, where W is the channel width) highly deviates from the unity.^{22,25,28,42,43,46–48} This reduction of equilibrium position compared with square microchannels makes rectangular microchannels widely employed in particle focusing and separation. However, six or even eight positions have also been observed in rectangular microchannels with similar AR .^{19,21} Such inconsistency indicates a lack of clear understanding of the focusing mechanism in rectangular microchannels.

To investigate the mechanism of the particle migration/focusing, several research groups performed analytical studies based on the perturbation methods.^{37–40,46,49–51} The inertial lift on the particle in a Poiseuille flow can be scaled as follows:^{38–40}

$$F_L = C_L \rho_f U_{\max} a^2 \kappa^2 \quad (1)$$

where C_L is a nondimensional lift coefficient. Asmolov calculated the lift forces on a particle in a planar Poiseuille flow with Re up to 3000,⁴⁰ showing that the equilibrium position shifts closer to the wall with increasing Re , which qualitatively agrees with the existing experimental results for both square^{42,45} and circular^{52,53} microchannels. However, applying these analytical results to practical applications is still difficult. The point-particle model ($\kappa \ll 1$) induces quite a large deviation for the particle with the same dimensional scale of the microchannel cross-section. Moreover, a planar Poiseuille flow model leads to zero forces in the perpendicular direction, whereas the lift force is a two-component vector in nature.

Direct numerical simulations (DNS) are able to relieve the restrictions of $\kappa \ll 1$ encountered in the perturbation theories.^{41,44,47,54–56} By conducting 3D DNS, Yang *et al.* obtained the lift forces on a sphere in a tube flow.⁴¹ The lift force at higher Re indicates two equilibria along the radial direction, which is consistent with the experimental observation of two rings in a tube flow by Matas *et al.*⁵² Using lattice Boltzmann methods, Chun *et al.* found eight equilibrium positions in square channels at $Re = 100$,⁴⁴ which is similar to the experimental observation by Bhagat *et al.*¹⁹ Di Carlo *et al.* numerically determined complicated scaling for the inertial lift force: $F_L \propto \rho_f U_{\max}^2 a^3 / H$ near the channel center, whereas $F_L \propto \rho_f U_{\max}^2 a^6 / H^3$ near the channel wall. Zhou *et al.* experimentally showed that the rotation-induced forces play an important role in particle migration toward the centers of the long walls in microchannels with high AR .⁵⁷ However, the rotation-induced force is always directed toward the center of the channel walls, and thus cannot explain the multiple equilibrium positions near the long walls. Gossett *et al.*

numerically investigated the inertial migration of particles at $Re = 80$ in a microchannel with $AR = 2$.²⁸ They found two stable equilibrium positions centered at the long walls and two unstable ones centered at the short walls, which is consistent with the existing experimental observation of focusing at the centers of the long walls. This research focuses on application and only performs the simulation for a single Re .

To better understand the mechanism of the inertial focusing behavior, we conduct 3D DNS and experiments to investigate the inertial migration of neutrally buoyant particles in microchannels within a wide parameter space. The equilibrium position can be classified into three types—stable, unstable or sub-stable depending on κ , AR and Re . By establishing the connection between the transformation of focusing patterns and the stability of equilibrium, we consequently eliminate the inconsistency among existing studies. Two mechanisms are further presented to explain the change of focusing behaviors in rectangular channels: stabilization of the originally unstable equilibrium positions near the centers of the short wall with increasing Re and the emergence of new equilibrium positions due to the dramatic change of the lift force profile near the long wall. Finally, we present a critical Reynolds number, Re_c , which is a function of AR and κ , to secure reduced focusing positions in rectangular microchannels.

Methods

Numerical models

The schematics in Fig. 1(a) shows that a rigid spherical particle with a diameter a is suspended in a rectangular Poiseuille

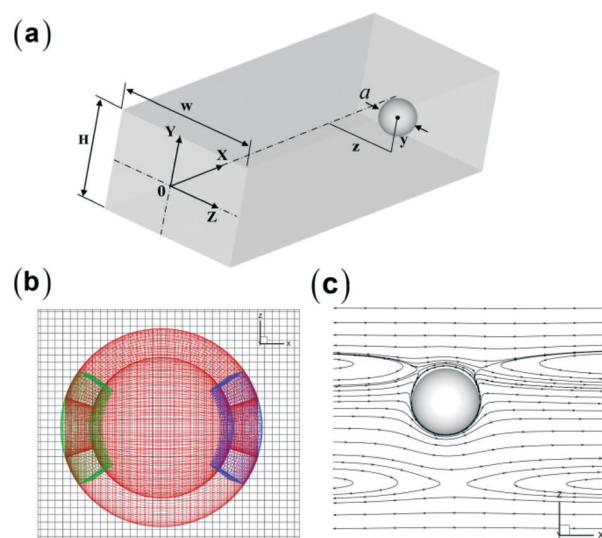


Fig. 1 (a) The schematics of the system and the set of the coordinate system. (b) The overlapping grid for a sphere in a rectangular microchannel consists of four component grids: the Cartesian grids for the channel (black), the body fitted grids for the sphere (red) and the grids for two poles (green and blue). (c) Streamlines in the $y = 0$ plane around the particle with $\kappa = 0.3$ at $Re = 100$ (in the reference frame fixed to the particle center).

flow. The origin of the coordinate system is located at the center of the channel inlet. The x -, y - and z -coordinates represent the main flow direction and the short and long axes of the cross-section, respectively.

The general function of the lift force on a neutrally buoyant particle in rectangular channels can be written as

$$F_L = F(a, y, z, H, W, U_{\max}, \eta, \rho_f) \quad (2)$$

Among the eight parameters, H , U_{\max} and ρ_f are used to nondimensionalize the system. According to the Buckingham pi theorem,⁵⁸ the general formula of lift force depends on five nondimensional quantities

$$F_L = F\left(\frac{a}{H}, \frac{y}{H}, \frac{z}{H}, 1, \frac{W}{H}, 1, \frac{\eta}{\rho_f U_{\max} H}, 1\right) = F(\kappa, y^*, z^*, AR, Re) \quad (3)$$

The κ determines the shear difference that the particle stretches over and the disturbance on the basic flow caused by the finite-size effect of the particle. The Re reflects the intensity of inertial nonlinearity of the undisturbed flow. The channel with an AR that deviates from the unity leads to a plug velocity profile along the long channel axis, which largely modifies the lift force distribution.⁴² A particle located at different lateral positions (y^* , z^*) will experience different hydrodynamic forces from the ambient flow that changes the lift force in magnitude or direction.

The governing equations (incompressible N-S equations for fluid flow and Newton's second law of motion for particle migration) are numerically solved on structured overlapping grids in the Overture C++ framework.⁵⁹ The no-slip wall boundary conditions are imposed on the channel walls and the surface of the particle. The Poiseuille-flow velocity profile for a rectangular cross-section is imposed on the inlet and fully developed flow conditions are imposed on the outlet. A second-order Adams predictor-corrector method is used for time stepping in solving the incompressible N-S equations.⁶⁰ The Poisson equation for pressure is implicitly solved to obtain vanishing divergence. The linear system derived from the pressure equation is iteratively solved using the stabilized bi-conjugate gradient method (BiCG-Stab) with the incomplete LU preconditioner (ILU). The solving process is done by using the PETSc software package that has an interface to the Overture framework.⁶¹ The elliptic type pressure equation is efficiently solved on the overlapping grid using the multigrid method. A more detailed procedure is given in sect. S1 of the ESI.†

Calculation of the lift force

To obtain the lift force at a certain lateral position in the channel, the particle is constrained to a line parallel to the mainstream (x -axis) with its lateral motion suppressed while the particle is allowed to freely rotate. The particle is static at the beginning of the simulation, and subsequently moves under the hydrodynamic forces and torques. When the translational and rotational motions both reach steady states, the lateral components (F_y and F_z) of the hydrodynamic force

acting on the particle are calculated as the lift force. This method has been previously used to obtain the lift force.^{28,41,42} By varying the lateral position and repeating the above procedures, we obtain the spatial distribution of the lift force, from which the equilibrium position and its stability can be determined.

Our simulation is validated by comparing our numerical results with the results from the existing work. Yang *et al.* conducted constrained simulation for a case of a sphere in a tube using the ALE code and the DLM code.⁴¹ The sphere is neutrally buoyant with $\kappa = 0.15$ and $Re = 100$. Our calculated lift forces agree well with Yang *et al.*'s results (Fig. S1†). We further test the grid independency by comparing the results of the above case using three grid resolution levels (Fig. S1†). The grid resolution is measured in the ratio of the size of the background grid Δx to the sphere diameter a . The very small difference among the results of the different grid resolutions indicates that the grid with $\Delta x/a = 0.1$ is adequate and thus employed through the present simulations.

Experiments

All the microchannels are 50 μm high and 60 mm long, with one inlet and one outlet. The entrance length required for a developed velocity profile is insignificant compared to the whole channel length (see sect. S2 in the ESI†). To study the effects of AR , we use four different widths of 50, 100, 200 and 300 μm , corresponding to four AR values of 1, 2, 4 and 6, respectively. The suspensions of 15 μm (green) and 5 μm (red) fluorescent polystyrene microspheres (Phosphorex Inc., USA) are diluted in deionized water to 10^6 particles mL^{-1} . To prevent particle aggregation, surfactant Tween 20 is added into the suspensions at 0.1 w/v%.

Liquid with polystyrene particles is injected into the straight microchannels using a syringe pump (Pump 11 Elite, Harvard Apparatus, USA). The flow rate is precisely adjusted by changing the parameters of the pump. The chip containing the microchannel is mounted onto the stage of a Leica DMI 6000 microscope (Leica Microsystems, Germany). Fluorescence streak images are taken by a CCD camera with an exposure time of 5 s. The images are taken at 60 mm from the inlet in a top view.

The microfluidic device is fabricated by the standard soft-lithography technique.^{15,20} The master mold is created on a silicon substrate mold by exposing the photoresist SU-8. After being peeled off from the mold, the polydimethylsiloxane (PDMS) slab is punched through to make ports at the inlet and outlet. The plastic tubes with a small amount of glue at their ends are inserted through the inlet and outlet ports. In contrast to the traditional procedure, a second layer of uncured PDMS is poured on the chip to cover the interconnection and the whole chip is baked in an oven at 80 $^{\circ}\text{C}$ for 2 h. This step makes the tubing interconnection sustain much higher pressure than traditional ones do.⁶² The PDMS slab is treated with oxygen plasma and then bonded to a glass substrate (25 mm \times 75 mm). Finally the assembled device is cured at 70 $^{\circ}\text{C}$ for 30 min to enhance bonding.

Results and discussion

Stabilization of the equilibrium at the short wall center

We numerically and experimentally study the focusing patterns of the particles with $\kappa = 0.1$ and 0.3 in a microchannel with $AR = 2$ at $Re = 100$ and 200 (Fig. 2). The lift force vectors are plotted for a quarter of the channel cross-section and the equilibrium positions are marked with circles. There are four equilibrium positions (where the lift forces vanish along both axes) centered at the four channel walls. For simplicity, the two equilibrium positions centered at the long walls are termed as long-wall-center equilibria (LWCE), and the other two centered at the short walls are termed as short-wall-center equilibria (SWCE).

To determine the stability of the equilibrium positions, we take a look at the lift force profile along both the long and the short axes crossing the equilibrium positions (Fig. 2e–h).

The positive lift force is directed towards the channel wall while the negative lift force is directed towards the channel center. The stability of the equilibrium is determined by the slope of the lift-coordinate curve at the equilibrium position (marked with black stars in Fig. 2e–h). The negative slope indicates a stable equilibrium because the particle will be pushed back to the equilibrium position once it is disturbed away from the position; on the contrary, the positive slope indicates an unstable equilibrium. The slopes along both axes around the LWCE are negative for all the cases (Fig. 2g–h), indicating that LWCE is stable and thus particles will focus at the centers of the long walls. This is consistent with the corresponding experimental observation of the middle streak in the top view for all the conditions (Fig. 2a–d).

In contrast to the LWCE, the SWCE is conditionally stable. For $\kappa = 0.3$, the SWCE is sub-stable (the equilibrium is stable only along the long axis.) at $Re = 100$ and becomes stable at

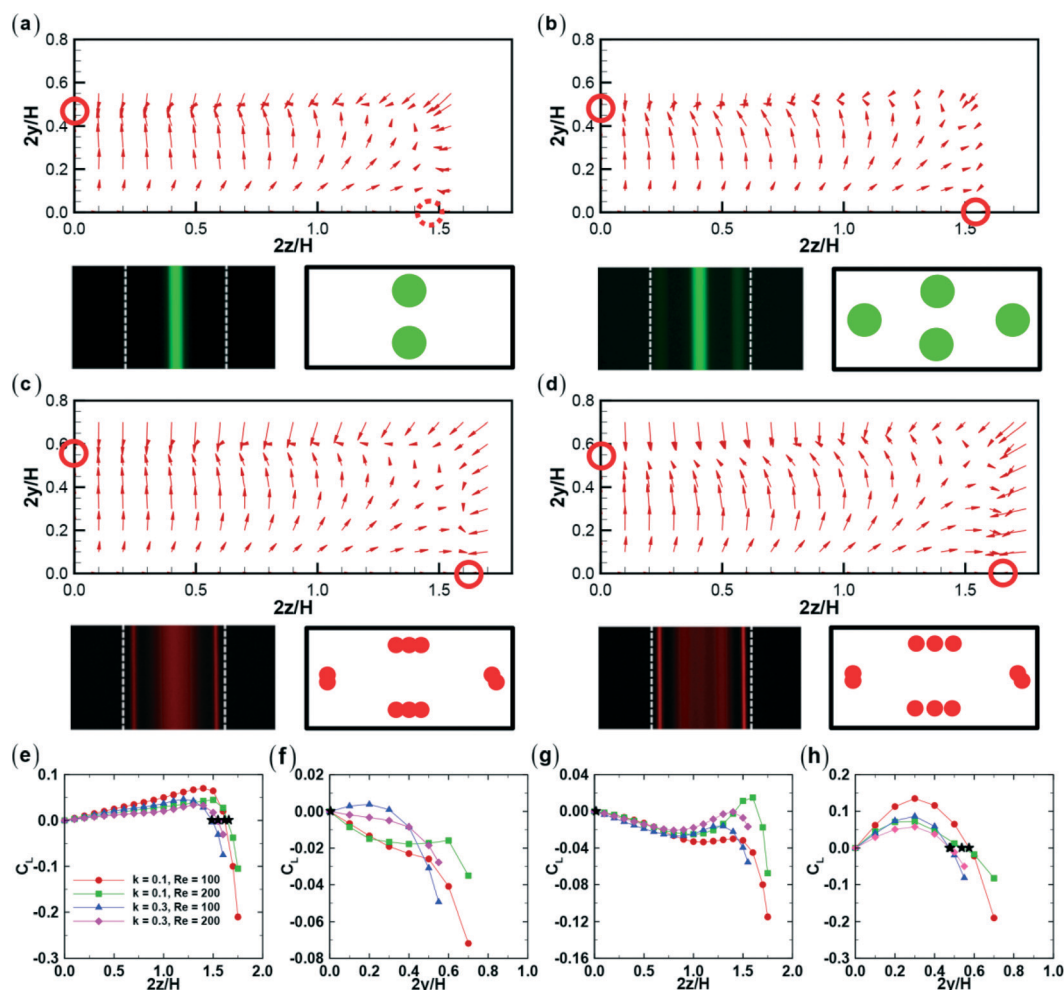


Fig. 2 The inertial lift distribution and fluorescence images of particle distribution in microchannels with $AR = 2$. The inertial lift forces are numerically calculated for a quarter of the channel cross-section and shown in the vector plots for particles with $\kappa = 0.3$ (a, b) and 0.1 (c, d) at $Re = 100$ (a, c) and 200 (b, d). In these vector plots, the solid-line circles indicate stable equilibrium positions and the dashed-line circles indicate unstable equilibrium positions. In the experimental images, fluorescent particles with diameters of $15\ \mu\text{m}$ ($\kappa = 0.3$, green) and $5\ \mu\text{m}$ ($\kappa = 0.1$, red) are flowing in a $100\ \mu\text{m}$ wide \times $50\ \mu\text{m}$ high microchannel. The lift force profiles are calculated for the long (e) and the short (f) axes crossing the short-wall-center equilibrium position (SWCE) and the long (g) and the short (h) axes crossing the long-wall-center equilibrium position (LWCE). The equilibrium positions are marked with black stars.

$Re = 200$ (Fig. 2e–f). The stabilization of the SWCE at $Re = 200$ is related to the reversal of sign for the slope along the short axis (Fig. 2f). To explain the reversal of sign, we take a look at the lift forces along the short axes F_y at various nondimensional coordinates $2z/H$ (Fig. 3). The lift forces on the short axis change little with $2z/H$ and the slopes are positive on the long main axis ($2y/H = 0$) near the center of the channel ($2z/H = 0-1.2$), indicating that no stable equilibrium forms near the channel center. When the particle moves close to the short wall ($2z/H = 1.2-1.55$), the lift forces largely change with increasing $2z/H$ and the slopes become negative on the long main axis, resulting in stable SWCE. The equilibrium position shifts toward the wall as Re increases.^{5,22,23,25} The SWCE for $\kappa = 0.3$ is at $2z/H = 1.49$ and 1.55 for $Re = 100$ and 200 , respectively (marked with black stars in Fig. 2e). The tendency toward the short wall at higher Re makes the SWCE lie at the negative-slope region and thus become stable. Under similar geometrical conditions, Prohm *et al.*⁶³ ($AR = 2$, $\kappa = 0.4$) and Gossett *et al.*²⁸ ($AR = 2$, $\kappa = 0.25$) did not report stable SWCE, probably because the Re in their simulation ($Re \sim 10$) was not high enough for obtaining stable SWCE (note that stable SWCE for $AR = 2$ and $\kappa = 0.3$ begins to be observed when $Re \approx 200$ in the present study).

Compared to the $\kappa = 0.3$ particles, the SWCE of the $\kappa = 0.1$ particles is stable at $Re = 100$ and 200 (Fig. 2e–f). The $\kappa = 0.1$ particles are closer to the channel walls than the $\kappa = 0.3$ particles at the same Re , and thus they always stay at the negative-slope region, resulting in stable SWCE. Fig. 4 shows the location and the stability of the SWCE for a wide parameter space ($\kappa = 0.1, 0.2$ and 0.3 , and $Re = 30, 60, 100, 200$ and 300). The results reveal the general dependence of SWCE stability on κ and Re : (1) the stabilization of SWCE occurs at Re higher than the critical value for every fixed κ , and (2) the critical Re increases with κ . This is because larger particles (larger κ) obtain equilibrium farther from the short wall, and thus the larger particles lie at the negative-slope region at higher Re .

Multiple equilibrium positions near the long wall at high Reynolds numbers

In this part, we will show that stable equilibrium positions will occur near the long channel walls in addition to the

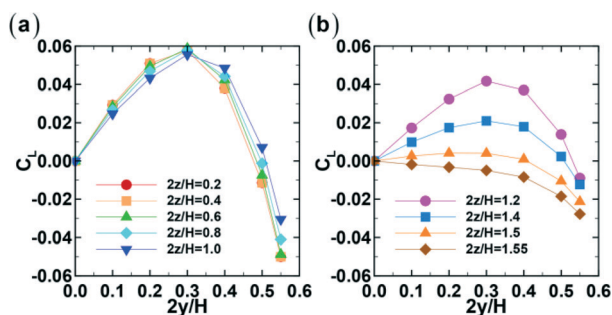


Fig. 3 The lift force profiles for particles with $\kappa = 0.3$ on short axes at various nondimensional coordinates $2z/H$ in a channel with $AR = 2$.

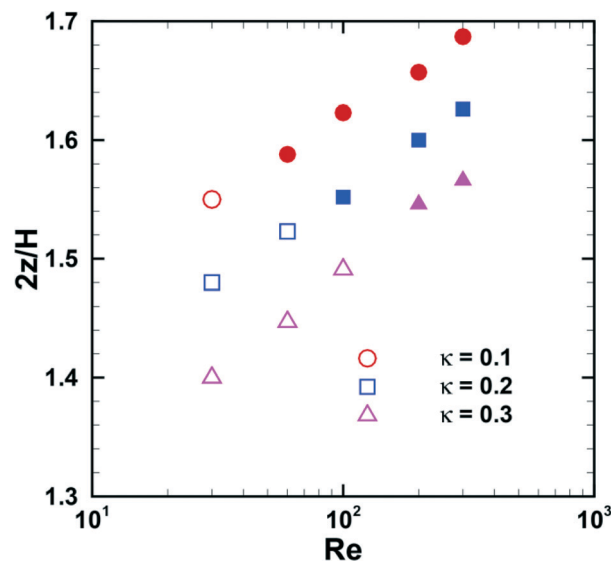


Fig. 4 The short-wall-center equilibrium positions (SWCE) shift towards the wall and tend to be stable with increasing Re . The solid marks indicate stable equilibrium positions, whereas the open marks indicate sub-stable equilibrium positions.

LWCE, which is related to the dramatic change of the lift force profile with increasing Re . The simulation conditions are $\kappa = 0.3$, $AR = 4$ and $Re = 50-300$. Instead of calculating lift forces for the whole cross-section, the equilibrium positions of particles are determined by the lift force profile along the long axis at certain $2y/H$. We first explain the reason for this simplification and then show how the change of the lift force profile leads to multiple equilibria and the underlying mechanism.

Fig. 5 shows that the F_y profile changes little in most part of the microchannel unless the particle is very close to the short wall and a stable equilibrium is obtained at nearly the same $2y/H$. The flow in the middle part of the channel with high AR is similar to a planar Poiseuille flow. The approximation of the planar Poiseuille flow is valid in 80% of the channel width for $AR = 4$. Therefore, it is reasonable and computationally economical to determine the final focusing position from the lift profile on the long axis rather than to calculate the lift forces for the entire cross-section.

On the long axis crossing the equilibrium position, F_z is a monotonically decreasing function of z and is negative on the entire axis at $Re = 50$. Such a lift force profile results in the focusing at the centers of the long walls (LWCE). However, the lift profile dramatically changes with increasing Re and the lift curve is no longer monotonic (Fig. 6). Between the center and the wall, the lift forces remarkably increase in magnitude with increasing Re from 100 to 300 , and form a second negative slope on the lift curve. At $Re = 300$, the sign for the lift force reverses into positive around $2z/H = 3.4$, leading to a stable equilibrium position between the positive peak and the wall.

The inertia of the high Re flow is responsible for the reversal of the sign for the lift force. The inviscid effect becomes

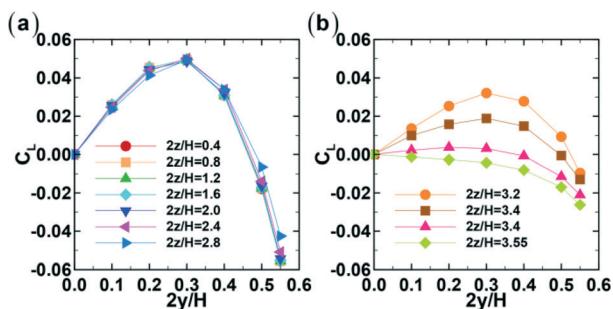


Fig. 5 The lift force profiles for $\kappa = 0.3$ particles on short axes at various nondimensional coordinates $2z/H$ in a channel with $AR = 4$.

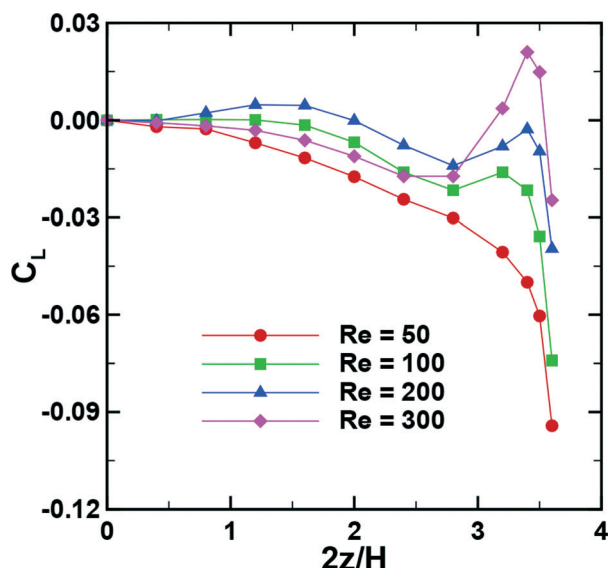


Fig. 6 The lift force profiles for $\kappa = 0.3$ particles in a channel with $AR = 4$ at various Re values ranging from 50 to 300. The lift force profiles dramatically change with increasing Re . The $2y/H$ values for the case of $Re = 50, 100, 200$ and 300 are $0.46, 0.48, 0.52$ and 0.55 , respectively (see Fig. S2 in the ESI†).

more important near the wall with increasing Re . The fluid between the particle and the wall is accelerated and thus leads to a Bernoulli-like effect, *i.e.*, low pressure at the wall side of the particle.⁶⁴ Pressure force dominates over the viscous force in the lateral migration of particles.^{47,65,66} Fig. 7 shows the pressure distribution on the surface of a sphere centered at $2z/H = 3.5$ and $2y/H = 0.55$ for $Re = 50$ and 300 in a microchannel with $AR = 4$. The nondimensional pressure coefficient is defined as $C_p = (p - p_\infty)/(0.5\rho_f U_{\max}^2 \kappa^2)$. There are four distinguished points on the sphere surface, two maxima at the windward side and two minima at the leeward side (in the reference frame fixed with the particle center) (see Fig. S3 in the ESI†). The pressure distribution becomes more asymmetrical for $Re = 300$ than that for $Re = 50$. The low-pressure region is much larger at the leeward side for $Re = 300$ because of the strong fluid inertia. The low pressure sucks the particle towards the side where it lies, whereas the high pressure pushes the particle away from the side where it lies. With increasing Re , the high-pressure regions slightly

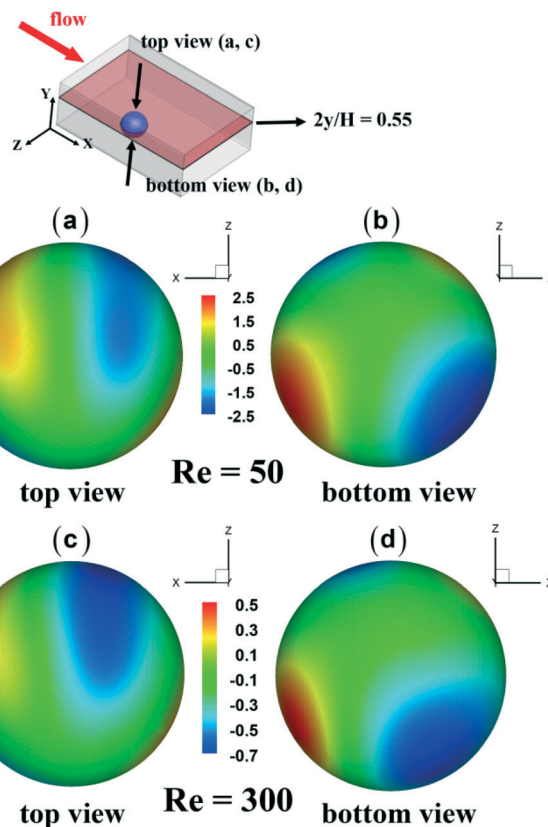


Fig. 7 The contour plot of the nondimensional pressure coefficient on the particle ($\kappa = 0.3$) surface with its center located at $2z/H = 3.5$ and $2y/H = 0.55$ for $Re = 50$ (a, b) and $Re = 300$ (c, d).

shrink and shift to the points that have larger angles with the z -axis, which makes the push effect less significant. The low-pressure regions at both the wall side and the center side expand, and these expand much more at the wall side, which leads to the net lift force in favor of the toward-wall motion for $Re = 300$.

Particle trajectories

Using the lift forces from DNS, we numerically predict the motion of particles starting at various positions in the cross-section (Fig. 8). The trajectories are derived from the integration of force balance based on Newton's second law of motion,

$$m_p \frac{du_p}{dt} = F_D + F_L + F_V \quad (4)$$

where F_D is the drag force, F_L is the lift force, and F_V is the virtual mass force that accelerate the surrounding fluid. More details can be found in our previous work.^{12,13}

We highlight two points about the particle migration drawn from the particle trajectories. First, the final equilibrium positions of particles depend on their initial positions. There is a separatrix that divides the cross-section into two parts. Particles starting between the separatrix and the nearest short wall will migrate to the SWCE, whereas particles starting at the other part of the cross-section will migrate

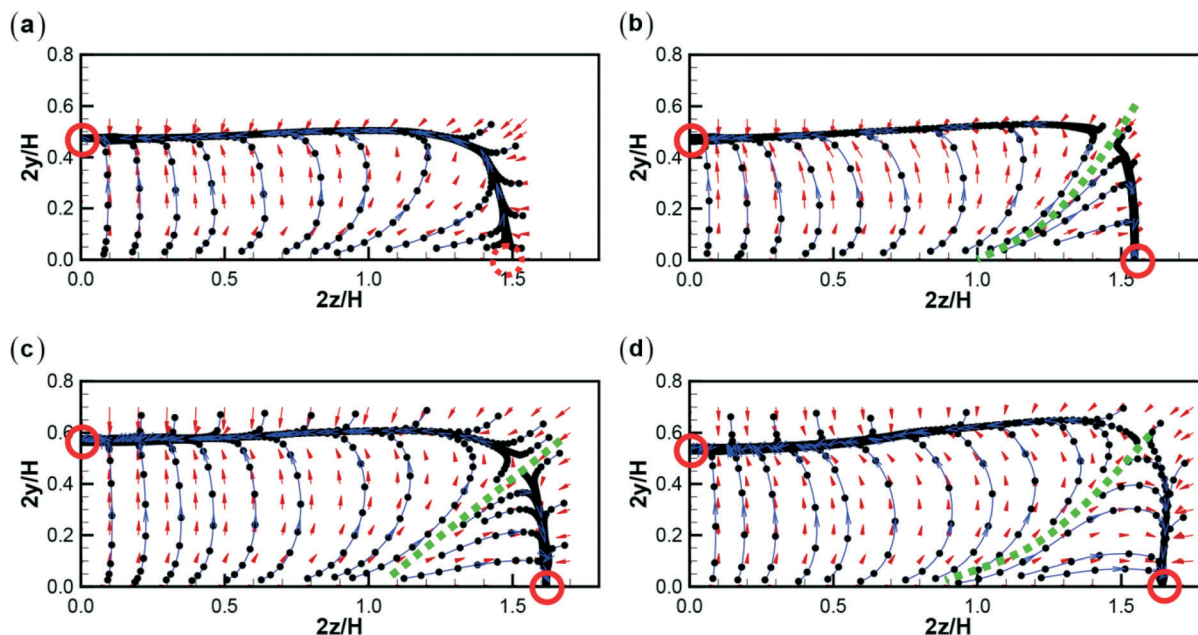


Fig. 8 The particle trajectories (blue lines) in a channel with $AR = 2$. The solid-line circles donate stable equilibrium positions and the dashed-line circles donate unstable equilibrium positions. The small black full circles are put on the trajectories every 200 nondimensional time units. The green dashed line is the separatrix dividing the cross-section into two parts, from which the particle starts which will focus at different equilibrium positions. The results for particles with $\kappa = 0.3$ (a, b) and $\kappa = 0.1$ (c, d) at $Re = 100$ (a, c) and 200 (b, d) are shown.

to the LWCE. The particles do not migrate straight to the wall, but with an incline to the other orthogonal wall. This is because the orthogonal wall also introduces the Poiseuille velocity profile and therefore the orthogonal component of the lift makes the particle move away from the straight path.

Second, the migration towards the equilibrium position is a two-step process. Particles predominately migrate away from the channel center and the walls, and therefore form a rectangular ring. The particles then migrate along the channel perimetric direction and finally focus at discrete equilibrium positions. The first step occurs much faster than the second step. The trajectories are marked by full circles every 200 nondimensional time units $t/t^*(t^* = (a/U_{\max})(6 \mu\text{m}/a)^4)$ to give an intuitive idea on how fast the migration is. The first step is similar to the inertial focusing into an annulus in a tube, dominated by the balance between the shear gradient force F_s and the wall effect F_w . After the two forces cancel each other out, rotational force F_Ω dominates the perimetric migration.⁶⁷ Since F_Ω is much weaker than F_s and F_w , the second step occurs slowly.^{57,68} The numerical results are consistent with the recent experimental observations of two-stage migration.^{16,57}

Lift force profile along the long main axis

The velocity profile along the long main axis tends to be plug-like in high AR channels. The reduced velocity curvature near the center can result in the change of lift forces in magnitude or direction. We calculate the lift profile on the long main axis for $AR = 2-6$, $\kappa = 0.2-0.8$ and $Re = 200$.

We categorize the lift curve on the long main axis by the number of negative slope since it is in favor of stable

equilibrium. One type is concave downwards in the entire line with only one negative slope that is located between the positive peak and the wall, which can be well predicted by the traditional model: the balance between the shear-gradient lift and the wall effect. The second type has two negative slopes at the near-center region and the near-wall region, respectively. Fig. 9 shows the dependence of the lift curve type on AR and κ . There is a separatrix dividing the AR- κ map into two parts. Under the conditions at the lower left of the separatrix, the lift curve has one negative slope. Under the conditions at the upper right, the lift curve has two negative slopes. Our numerical results reveal that when AR is fixed, the negative slope near the channel center occurs when κ exceeds a certain critical value, and the critical κ decreases with increasing AR.

The negative slope near the channel center is due to the sign reversal of the previously positive lift force, which can be attributed to the finite size effect of particles. Neutrally buoyant particles with finite size can slightly lag behind the ambient flow.^{41,47} The lift forces tend to push the particle to the channel center when the particle lags behind the ambient fluid.^{37,47,69} The difference between the undisturbed flow velocity at the particle center and the particle velocity is termed as slip velocity, which scales as $U_{\max}\kappa^2$ (ref. 70). In contrast to a small particle ($\kappa \ll 1$) with vanishing slip velocity, a finite size particle has an observable slip velocity that increases with the particle size. Therefore, the negative slope near the channel center tends to occur for high κ . The shear gradient effect is eliminated near the channel center due to the diminished curvature in high AR channels, which is in favor of negative lift forces. Consequently, the lift force due

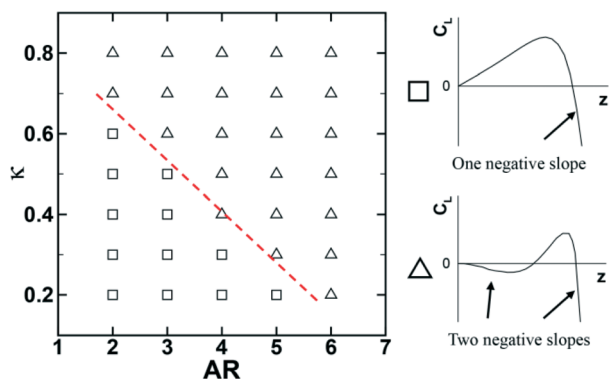


Fig. 9 The dependence of the patterns of lift force profiles along the long main axis on κ and AR at $Re = 200$.

to the slip velocity easily overcomes the weak wall-direct shear gradient effect and thus leads to the negative slope near the channel center in channels with higher AR. Therefore, the critical κ decreases with increasing AR.

Experimental validation and a design criterion

The focusing behaviors of particles with diameters of $5\ \mu\text{m}$ and $15\ \mu\text{m}$ ($\kappa = 0.1$ and 0.3 , respectively) are experimentally observed in microchannels with AR values of 1, 2, 4 and 6 under various flow rates corresponding to $30 \leq Re \leq 468$.

In square microchannels, the particles focus at the four equilibrium positions centered at the channel walls for every investigated Re ($117 \leq Re \leq 468$) (Fig. 10(a)), which is consistent with previous observations at $Re \sim 100$.^{45,67} A very recent experiment by Lim *et al.* showed the focusing of $\kappa = 0.1$ particles at the four channel corners at $Re = 1400$ in epoxy-based microchannels. The focusing at the channel corners is not observed in the present study, because this focusing pattern only occurs at a very high Re .

In high AR ($AR \geq 2$) microchannels, the focusing behaviors are dependent on Re in a complicated manner. When Re is near the low limit of our experiments, the $15\ \mu\text{m}$ particles focus at the centers of the long walls, in agreement with the present numerical prediction. When the flow rate reaches $40\ \text{mL h}^{-1}$ ($Re = 220$), a small part of the particles focus near the side walls. The corresponding image shows two barely visible streaks near the side walls. When the flow rate exceeds $60\ \text{mL h}^{-1}$ ($Re = 330$), more particles focus near the side walls. The emergence of side streaks arises from the equilibrium turning stable at higher Re , which is consistent with the above discussion. The $5\ \mu\text{m}$ particles form a wide band in the middle of the microchannel when the flow rate is $20\ \text{mL h}^{-1}$ ($Re = 110$). There is a tendency to achieve a narrower middle streak and two side streaks (like the $15\ \mu\text{m}$ particles do) as the Re increases. The reason of the insufficient focusing of the $5\ \mu\text{m}$ particles within the fixed channel length is that the lift forces acting on them are too weak, since the inertial lift force scales as $F_L \propto a^4$. In contrast to the $15\ \mu\text{m}$ particles, $5\ \mu\text{m}$ particles form two side streaks

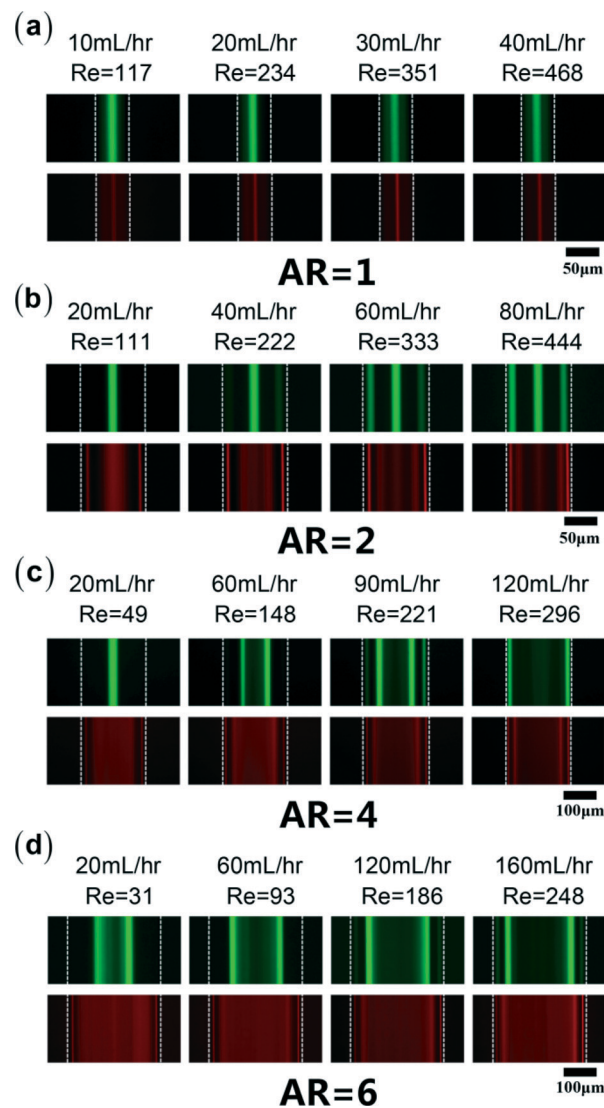


Fig. 10 Fluorescence images taken at the 60 mm downstream of the inlet in the top view showing the focusing behaviors of $5\ \mu\text{m}$ (red) and $15\ \mu\text{m}$ (green) particles under various flow rates for AR = 1 (a), AR = 2 (b), AR = 4 (c) and AR = 6 (d).

near the side walls for every investigated Re , which is again consistent with our prediction. The reduction of the equilibrium number in rectangular microchannels is achieved when Re is below the critical value.

In microchannels with AR = 4 and 6, the focusing behaviors of particles cannot be predicted by simply stretching the results of microchannels with AR = 2. For the lowest Re , the $15\ \mu\text{m}$ particles focus into a narrow streak in the microchannel with AR = 4. At a higher Re , however, the $15\ \mu\text{m}$ particles form two streaks located symmetrically at the channel centerline, which is always different from the existence of the middle streak when AR = 2. The two streaks are closer to the side walls with increasing flow rates. When the flow rate is $120\ \text{mL h}^{-1}$ ($Re = 296$), the two streaks are very close to the side walls. The transformation of the particle's focusing behaviors is consistent with the calculated lift profile along

the axis crossing the equilibrium position (Fig. 6). The 5 μm particles form a wide band in the middle of the microchannels with $\text{AR} = 4$ and 6 for every investigated Re . More particles migrate to the edges of the wide band with increasing Re , indicating a tendency to form two symmetrical streaks like 15 μm particles.

High AR microchannels can reduce the number of equilibrium positions (two equilibrium positions centered at the long walls) compared to square microchannels (four centered at the channel walls). However, the number of stable equilibrium positions will increase when Re exceeds a certain critical value. The critical Re is a function of AR and κ . For small κ , the short-wall equilibrium emerges at lower Re . In microchannels with higher AR, the plug-like velocity profile makes the lift profile likely to form multiple stable equilibrium. Therefore, we use a tentative parameter AR/κ to evaluate the accessibility of a reduced number of equilibrium positions. Using the experimental results from previous studies and ours, the critical Re is determined as $\text{Re}_c = 697(\text{AR}/\kappa)^{-0.79}$ ($4.5 \leq \text{AR}/\kappa \leq 60$, $5 \leq \text{Re} \leq 660$) (Fig. 11). Therefore, we can eliminate the inconsistency of different focusing positions reported by previous studies on rectangular microchannels. For example, in Bhagat *et al.*'s experiments, AR/κ is obviously higher than that used in other studies; therefore it is easier for them to observe more than two equilibrium positions at $\text{Re} > \text{Re}_c$, whereas many other researchers use a relatively low value of AR/κ and thus high Re is needed to obtain additional equilibrium positions.

Conclusions

In the present work, we investigate the number and the locations of the equilibrium positions in a wide parameter space using DNS and experiments. In contrast to the traditional

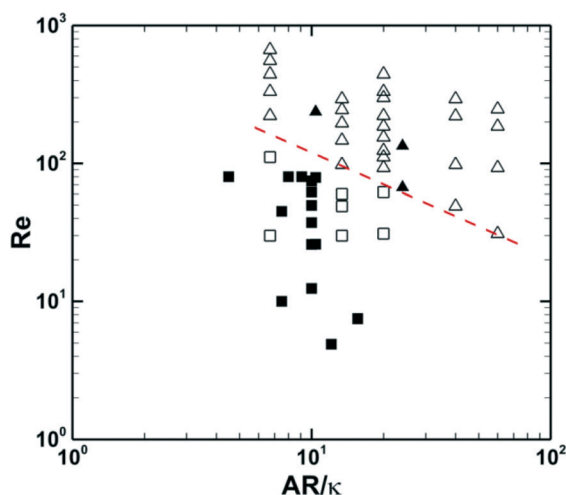


Fig. 11 The dependence of particle focusing patterns on AR, κ and Re . Focusing into one streak at the channel midline in the top view (focusing at the centers of the long walls) corresponds to squares, and focusing into multiple streaks or no focusing corresponds to triangles. Open marks are results from the present study and filled marks are those from the existing studies.^{8,21,28,42,43,67,71–73}

knowledge of focusing at the centers of the long walls, we numerically demonstrate new stable equilibrium positions in a rectangular channel, which is validated by experimental observation. The new stable equilibrium positions can occur by two mechanisms: 1) the stabilization of the originally unstable or sub-stable equilibrium positions near the centers of the short wall by the increasing Re , and 2) the emergence of new stable equilibrium positions due to the attractive lift forces near the long wall at a high Re , which is a Bernoulli-type effect. With the same AR, the critical Re to obtain the new stable equilibrium positions decreases with the particle size κ , and the critical Re also decreases with AR for fixed κ .

In practice, both the reduction of equilibrium positions and the high throughput are desirable for the inertial microfluidic applications. However, the present study indicates that the focusing performance can degrade if the flow rate is too high. Based on the numerical calculations and experimental data, we propose a critical $\text{Re}_c = 697(\text{AR}/\kappa)$ for good focusing at a high throughput.

Acknowledgements

We thank the Ministry of Science and Technology (2011CB707604 and 2013AA032204) and the National Science Foundation of China (11272321, 21475028, and 51105086) for financial support. We sincerely thank Dr. William D. Henshaw for making the finite-difference code – overtone available to us. The numerical simulations were performed on TianHe-1(A) at the National Supercomputing Center in Tianjin.

Notes and references

- 1 Y. Kang, D. Li, S. Kalams and J. Eid, *Biomed. Microdevices*, 2008, **10**, 243–249.
- 2 J. Voldman, *Annu. Rev. Biomed. Eng.*, 2006, **8**, 425–454.
- 3 J. Zhu and X. Xuan, *Electrophoresis*, 2009, **30**, 2668–2675.
- 4 S. Miltenyi, W. Müller, W. Weichel and A. Radbruch, *Cytometry*, 1990, **11**, 231–238.
- 5 J. J. Hawkes, R. W. Barber, D. R. Emerson and W. T. Coakley, *Lab Chip*, 2004, **4**, 446–452.
- 6 F. Petersson, L. Åberg, A.-M. Swärd-Nilsson and T. Laurell, *Anal. Chem.*, 2007, **79**, 5117–5123.
- 7 D. Di Carlo, D. Irimia, R. G. Tompkins and M. Toner, *Proc. Natl. Acad. Sci. U. S. A.*, 2007, **104**, 18892–18897.
- 8 J. Zhang, S. Yan, W. Li, G. Alici and N.-T. Nguyen, *RSC Adv.*, 2014, **4**, 33149–33159.
- 9 J. Zhang, S. Yan, R. Sluyter, W. Li, G. Alici and N.-T. Nguyen, *Sci. Rep.*, 2014, **4**.
- 10 D. Di Carlo, J. F. Edd, D. Irimia, R. G. Tompkins and M. Toner, *Anal. Chem.*, 2008, **80**, 2204–2211.
- 11 A. A. S. Bhagat, H. W. Hou, L. D. Li, C. T. Lim and J. Han, *Lab Chip*, 2011, **11**, 1870–1878.
- 12 J. S. Sun, M. M. Li, C. Liu, Y. Zhang, D. B. Liu, W. W. Liu, G. Q. Hu and X. Y. Jiang, *Lab Chip*, 2012, **12**, 3952–3960.
- 13 J. S. Sun, C. Liu, M. M. Li, J. D. Wang, Y. L. Xianyu, G. Q. Hu and X. Y. Jiang, *Biomicrofluidics*, 2013, **7**.

- 14 J. Zhou, P. V. Giridhar, S. Kasper and I. Papautsky, *Lab Chip*, 2013, **13**, 1919–1929.
- 15 A. J. Chung, D. R. Gossett and D. Di Carlo, *Small*, 2013, **9**, 685–690.
- 16 N. Xiang, K. Chen, Q. Dai, D. Jiang, D. Sun and Z. Ni, *Microfluid. Nanofluid.*, 2014, 1–11.
- 17 J. Oakey, R. W. Applegate, E. Arellano, D. Di Carlo, S. W. Graves and M. Toner, *Anal. Chem.*, 2010, **82**, 3862–3867.
- 18 A. J. Chung, D. Pulido, J. C. Oka, H. Amini, M. Masaeli and D. Di Carlo, *Lab Chip*, 2013, **13**, 2942–2949.
- 19 A. A. S. Bhagat, S. S. Kuntaegowdanahalli and I. Papautsky, *Phys. Fluids*, 2008, **20**, 101702.
- 20 J. Seo, M. H. Lean and A. Kole, *Appl. Phys. Lett.*, 2007, **91**, 033901.
- 21 A. A. S. Bhagat, S. S. Kuntaegowdanahalli and I. Papautsky, *Microfluid. Nanofluid.*, 2009, **7**, 217–226.
- 22 A. J. Mach and D. Di Carlo, *Biotechnol. Bioeng.*, 2010, **107**, 302–311.
- 23 A. A. S. Bhagat, *Ph.D. Thesis*, University of Cincinnati, 2009.
- 24 S. C. Hur, A. J. Mach and D. Di Carlo, *Biomicrofluidics*, 2011, **5**.
- 25 S. C. Hur, N. K. Henderson-MacLennan, E. R. B. McCabe and D. Di Carlo, *Lab Chip*, 2011, **11**, 912–920.
- 26 J. S. Dudani, D. R. Gossett, H. T. K. Tse and D. Di Carlo, *Lab Chip*, 2013, **13**, 3728–3734.
- 27 D. R. Gossett, H. T. K. Tse, S. A. Lee, Y. Ying, A. G. Lindgren, O. O. Yang, J. Rao, A. T. Clark and D. Di Carlo, *Proc. Natl. Acad. Sci. U. S. A.*, 2012, **109**, 7630–7635.
- 28 D. R. Gossett, H. T. K. Tse, J. S. Dudani, K. Goda, T. A. Woods, S. W. Graves and D. Di Carlo, *Small*, 2012, **8**, 2757–2764.
- 29 H. Amini, E. Sollier, M. Masaeli, Y. Xie, B. Ganapathysubramanian, H. A. Stone and D. Di Carlo, *Nat. Commun.*, 2013, **4**, 1826.
- 30 J. Zhang, M. Li, W. H. Li and G. Alici, *J. Micromech. Microeng.*, 2013, **23**, 13.
- 31 M. G. Lee, J. H. Shin, C. Y. Bae, S. Choi and J.-K. Park, *Anal. Chem.*, 2013, **85**, 6213–6218.
- 32 G. F. Guan, L. D. Wu, A. A. S. Bhagat, Z. R. Li, P. C. Y. Chen, S. Z. Chao, C. J. Ong and J. Y. Han, *Sci. Rep.*, 2013, **3**.
- 33 S. S. Kuntaegowdanahalli, A. A. S. Bhagat, G. Kumar and I. Papautsky, *Lab Chip*, 2009, **9**, 2973–2980.
- 34 N. Xiang, K. Chen, D. Sun, S. Wang, H. Yi and Z. Ni, *Microfluid. Nanofluid.*, 2013, **14**, 89–99.
- 35 G. Segré and A. Silberberg, *Nature*, 1961, **189**, 209–210.
- 36 F. P. Bretherton, *J. Fluid Mech.*, 1962, **14**, 284–304.
- 37 P. G. Saffman, *J. Fluid Mech.*, 1965, **22**, 385–400.
- 38 B. P. Ho and L. G. Leal, *J. Fluid Mech.*, 1974, **65**, 365–400.
- 39 J. A. Schonberg and E. J. Hinch, *J. Fluid Mech.*, 1989, **203**, 517–524.
- 40 E. S. Asmolov, *J. Fluid Mech.*, 1999, **381**, 63–87.
- 41 B. H. Yang, J. Wang, D. D. Joseph, H. H. Hu, T. W. Pan and R. Glowinski, *J. Fluid Mech.*, 2005, **540**, 109.
- 42 D. Di Carlo, J. Edd, K. Humphry, H. Stone and M. Toner, *Phys. Rev. Lett.*, 2009, 102.
- 43 S. C. Hur, H. T. K. Tse and D. Di Carlo, *Lab Chip*, 2010, **10**, 274–280.
- 44 B. Chun and A. J. C. Ladd, *Phys. Fluids*, 2006, **18**, 031704.
- 45 Y.-S. Choi, K.-W. Seo and S.-J. Lee, *Lab Chip*, 2011, **11**, 460.
- 46 P. Vasseur and R. G. Cox, *J. Fluid Mech.*, 1976, **78**, 385–413.
- 47 J. Feng, H. H. Hu and D. D. Joseph, *J. Fluid Mech.*, 1994, **277**, 271–301.
- 48 J. F. Edd, D. Di Carlo, K. J. Humphry, S. Koster, D. Irimia, D. A. Weitz and M. Toner, *Lab Chip*, 2008, **8**, 1262–1264.
- 49 J. B. McLaughlin, *J. Fluid Mech.*, 1991, **224**, 261–274.
- 50 J. B. McLaughlin, *J. Fluid Mech.*, 1993, **246**, 249–265.
- 51 P. Cherukat and J. B. McLaughlin, *J. Fluid Mech.*, 1994, **263**, 1–18.
- 52 J.-P. Matas, J. F. Morris and É. Guazzelli, *J. Fluid Mech.*, 2004, **515**, 171–195.
- 53 Y.-S. Choi and S.-J. Lee, *Microfluid. Nanofluid.*, 2010, **9**, 819–829.
- 54 H. H. Hu, D. D. Joseph and M. J. Crochet, *Theor. Comput. Fluid Dyn.*, 1992, **3**, 285–306.
- 55 H. H. Hu, *Int. J. Multiphase Flow*, 1996, **22**, 335–352.
- 56 H. H. Hu, N. A. Patankar and M. Y. Zhu, *J. Comput. Phys.*, 2001, **169**, 427–462.
- 57 J. Zhou and I. Papautsky, *Lab Chip*, 2013, **13**, 1121–1132.
- 58 T. QM, *Dimensional analysis: with case studies in mechanics*, Springer-Verlag, Berlin Heidelberg, 2011.
- 59 D. L. Brown, W. D. Henshaw and D. J. Quinlan, *Overture: An object-oriented framework for solving partial differential equations*, 1997.
- 60 W. D. Henshaw, *J. Comput. Phys.*, 1994, **113**, 13–25.
- 61 W. D. Henshaw and P. Fast, *Technical Report LA-UR-96-3468*, Los Alamos National Laboratory, 1998.
- 62 J. Wang, W. Chen, J. Sun, C. Liu, Q. Yin, L. Zhang, Y. Xianyu, X. Shi, G. Hu and X. Jiang, *Lab Chip*, 2014, **14**, 1673–1677.
- 63 C. Prohm and H. Stark, *Lab Chip*, 2014, **14**, 2115–2123.
- 64 Q. Liu and A. Prosperetti, *J. Fluid Mech.*, 2010, **657**, 1–21.
- 65 P. Y. Huang, J. Feng and D. D. Joseph, *J. Fluid Mech.*, 1994, **271**, 1–16.
- 66 L. Zeng, S. Balachandar and P. Fischer, *J. Fluid Mech.*, 2005, **536**, 1–25.
- 67 E. J. Lim, T. J. Ober, J. F. Edd, G. H. McKinley and M. Toner, *Lab Chip*, 2012, **12**, 2199–2210.
- 68 P. Bagchi and S. Balachandar, *Phys. Fluids*, 2002, **14**, 2719.
- 69 J. P. Matas, J. F. Morris and E. Guazzelli, *Oil Gas Sci. Technol.*, 2004, **59**, 59–70.
- 70 A. Leshansky, A. Bransky, N. Korin and U. Dinnar, *Phys. Rev. Lett.*, 2007, 98.
- 71 W. D. Henshaw and D. W. Schwendeman, *J. Comput. Phys.*, 2006, **216**, 744–779.
- 72 K. J. Humphry, P. M. Kulkarni, D. A. Weitz, J. F. Morris and H. A. Stone, *Phys. Fluids*, 2010, **22**, 081703.
- 73 J. M. Martel and M. Toner, *Sci. Rep.*, 2013, **3**.